Polymer−Nanoparticle Complexes: From Dilute Solution to Solid State

Jean-François Berret*

Matière et Systèmes Complexes, UMR CNRS no. 7057, Université Denis Diderot Paris-VII, 140 rue de Lourmel, 75015 Paris, France

Kazuhiko Yokota

Rhodia, Centre de Recherches d'Aubervilliers, 52 rue de la Haie Coq, 93308 Aubervilliers Cedex, France

Mikel Morvan

Complex Fluids Laboratory, UMR CNRS-Rhodia 166, Cranbury Research Center Rhodia, 259 Prospect Plains Road, Cranbury, New Jersey 08512

Ralf Schweins

Institute Laue-Langevin, LSS Group, BP 156, F-38042 Grenoble Cedex 9, France

Received: January 17, 2006; In Final Form: July 6, 2006

We report on the formation and the structural properties of "supermicellar" aggregates made from mineral nanoparticles and polyelectrolyte−neutral block copolymers in aqueous solutions. The mineral particles put under scrutiny are ultrafine and positively charged yttrium hydroxyacetate nanoparticles. Combining light, neutron, and X-ray scattering experiments, we have characterized the sizes and the aggregation numbers of the organic−inorganic complexes. We have found that the hybrid aggregates have typical sizes in the range of 100 nm and exhibit a remarkable colloidal stability with respect to ionic strength and concentration variations. Solid films with thicknesses up to several hundreds of micrometers were cast from solutions, resulting in a bulk polymer matrix in which nanoparticle clusters are dispersed and immobilized. It was found in addition that the structure of the complexes remains practically unchanged during film casting.

I. Introduction

Development of molecular architectures is one of the final goals of modern chemistry, physics, and biology. The emergence of novel materials and processing at the nano scale has enabled the synthesis of new materials, as well as provided decisive breakthroughs in the field of the nanotechnology.[1−4] This is the case of magnetic and luminescent nanocrystals which physical properties are nowadays exploited for imaging complex fluids at mesoscopic scales. In biomedicine, the particles can also be functionalized with ligands, peptides, and oligonucleotides to reach a target or to deliver a drug to a specific location.[5−7] One of the most promising approaches for the stabilization of nanoparticles in different environments such as in solutions and thin or thick films is based on the use of polymers or of copolymers. In solutions, the first objective is to build around the particle a diffuse and protective corona. This corona aims to promote purely steric repulsions between the colloids, reducing at the same time the range and strength of the electrostatic and van der Waals interactions.[8−10] Nowadays, polymer-coated nanoparticles can be obtained by in situ polymerization[8,9,11] or by encapsulation into block copolymer micelles.[12−17] Polymer coatings also can be achieved by simple physical-chemistry techniques based on electrostatic complexation between oppositely charged particles and polymers. Two protocols have been designed and reported so far. In the first one, polyelectrolyte−neutral block copolymers were associated in aqueous solutions with oppositely charged surfactants or nanoparticles, yielding the formation of stable and monodisperse "supermicellar" aggregates with core−shell structures.[18−21] In a second protocol, a two-step mechanism based on precipitation−redispersion of the mixed solutions was developed.[22] As an outcome of this second process, the particles are irreversibly coated with short homopolyelectrolyte chains, resulting in an increased stability for the solutions.

In the present paper, we re-examine the collective complexation investigated with use of neutral−charged diblocks and we apply it to yttrium hydroxyacetate (YHA) nanoparticles.[18,19] The YHA particles were chosen as a model system for inorganic colloids. Their typical sizes (∼2 nm) and charges compare well with those of cationic surfactant micelles, a colloidal system that was thoroughly investigated with respect to complexation during the past decade.[23−28] The YHA nanoparticles were also considered because of their potential applications as precursors for ceramic and optoelectronic materials.[29] In our earlier accounts on the YHA−diblock mixed systems, we had demonstrated the analogy between surfactant micelles and nanoparticles in the complexation phenomenon.[18,19] In the present report, we stress the similarities between the nanostructures formed by spontaneous electrostatic complexation and the polymeric micelles built from amphiphilic copolymers.[30] We are taking advantage of the enhanced stability of the YHA−diblock complexes to cast micrometer thick films from the

* Address correspondence to this author. E-mail: jean-francois.berret@paris7.jussieu.fr. Phone: 33 (0)1-44-27-44-97. Fax: 33 (0)1-44-27-38-82.

10.1021/jp0603177 CCC: $33.50
Published on Web 09/12/2006

solutions, as this is commonly done with copolymers in selective solvent.[31−34] The result of the film casting is a nanocomposite material made from clusters of nanoparticles dispersed in a polymer matrix.

II. Experimental Section

II.1. Characterization, Sample Preparation, and Phase Diagram. *Polyelectrolyte−Neutral Diblock Copolymer*. The poly(acrylic acid)-*b*-poly(acrylamide) block copolymers used to complex YHA nanoparticles were synthesized by controlled radical polymerization.[35,36] In the present study, we focus on the two polymers, PANa(5K)-*b*-PAM(30K) and PANa(5K)-*b*-PAM(60K), where PANa stands for poly(sodium acrylate) and PAM for poly(acrylamide). The values in parentheses are the molecular weights targeted by the synthesis of the acid forms. Although the actual values are slightly different (see below), they will be used throughout the paper. In aqueous solutions, the chains are well dispersed and in the state of unimers (pH >3). The weight-averaged molecular weights M_w^{pol} and the hydrodynamic radius R_H^{pol} were determined by static and dynamic light scattering (Brookhaven BI-9000AT spectrometer). We found $M_w^{pol} = 43\,500$ g·mol^{-1}, $R_H^{pol} = 5.5$ nm for PANa-(5K)-*b*-PAM(30K)and $M = 68\,300$ g·mol^{-1}, R_H^{pol} 7.9 nm for PANa(5K)-*b*-PAM(60K). The polydispersity index was determined by size exclusion chromatography at 1.6. Poly(acrylic acid) is a weak polyelectrolyte and its ionization state depends on the pH. To derive the molecular weight of the acrylic acid block, titration experiments were performed. By slow addition of 0.1 N sodium hydroxide, the pH of PANa-*b*-PAM solutions was varied from acidic to basic conditions. The determination of the titration curves and equivalences allowed us to obtain the degree of polymerization for the anionic block. We obtained $n_{PE} = 90$ for PANa(5K)-*b*-PAM(30K) and $n_{PE} = 77$ for PANa-(5K)-*b*-PAM(60K), yielding molecular weights of 6500 and 5560 g·mol^{-1}, respectively. Supplementary information for these polymers is available in ref 28.

Inorganic Nanoparticles. The synthesis of the yttrium hydroxyacetate (YHA) nanoparticles is based on a reaction described in refs 18 and 19. By the end of the reaction, the average composition of the particles is $Y(OH)_{1.7}(CH_3COO)_{1.3}$. As for the polymers, the molecular weight M_w^{nano} (=27 000 g·mol^{-1}) and the hydrodynamic radius R_H^{nano} (∼2 nm) of YHA nanoparticles were determined by light scattering. Zeta potential measurements (Zetasizer 3000 from Malvern) corroborate that the particles are positively charged ($\zeta = +45$ mV) and that the suspensions are stabilized by surface charges. The stability of $Y(OH)_{1.7}(CH_3COO)_{1.3}$ sols at neutral pH is excellent over a period of several weeks.

Sample Preparation and Phase Diagram. The mixed aggregates were obtained by mixing nanoparticle and polymer solutions prepared at the same weight concentration c ($c \sim 1$ wt %) and at the same pH (pH 7). The mixing ratio X is defined as the volume of yttrium-based suspension relative to that of the polymer. According to the above definitions, the concentrations in nanoparticles and polymers in the mixed solutions are $c_{pol} = c/(1 + X)$ and $c_{nano} = Xc/(1 + X)$. In earlier reports on nanoparticle−polymer complexes, we have shown that there exists a preferred mixing ratio noted X_P at which all the polymers and nanoparticles brought by mixing are involved in the formation of the hybrid colloids. For PANa-*b*-PAM/YHA complexes, X_P is around 0.2.[19]

Figure 1 shows a schematic phase diagram for the ternary system comprising copolymers, nanoparticles, and solvent. Solutions obtained according to the mixing procedure described above are located on the *X*-line. On the *X*-line, X varies from $X = 0$ to ∞, with the total concentration being constant. On the other hand, the *c*-line describes solutions at the same X, but with different concentrations. In this work, we have explored ranges in the mixing ratio X varying from 0 to ∞ and in concentration $c = 0.1$ to ∼100 wt % (solid state). The polymer−nanoparticle complexes were prepared at low concentrations, usually $c = 0.1-1$ wt %, and then concentrated by solvent evaporation or by ultrafiltration. The ultrafiltration cell was equipped with a 3000 g·mol^{-1} pore size filter (Pall Life Sciences). With increasing concentrations, the mixed systems pass from Newtonian liquids ($c < 30$ wt %) to viscoelastic gels ($c > 30$ wt %) and to solid. For the casting, open Teflon cells designed to contain up to $2 \times 2 \times 0.5$ cm^3 of liquid were filled with the solutions and stored at 60 °C during 1 day and under vacuum (0.01 atm). These conditions allowed for a slow evaporation of the solvent. Thermal Gravimetry Analysis (TGA) performed on the films has revealed the presence of unbound water molecules of nearly 10 wt %, i.e., the solid films have an actual concentrations of ∼90 wt %.

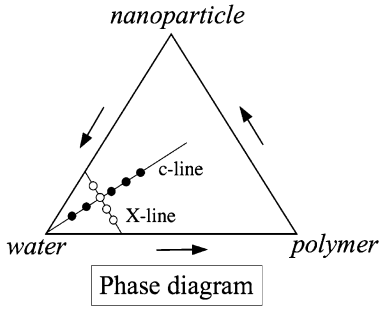

Figure 1. Schematic phase diagram for the ternary system comprising copolymers, nanoparticles, and water. The mixing procedures developed here provide solutions located on the *X*- and on the *c*-lines, X being the mixing ratio and c the total concentration. Here, we explore ranges in mixing ratios $X = 0-\infty$ and in concentrations $c = 0.1-90$ wt %.

II.2. Small-Angle Scattering. Static and dynamic light scattering were performed on a Brookhaven spectrometer for measurements of the Rayleigh ratio (absolute scattering intensity) and of the collective diffusion constant using an experimental setup described previously.[19] Light scattering was used to determine the apparent molecular weight $M_{w,app}$ of polymers, nanoparticles, and hybrids, as well as the radius of gyration R_G of the supermicellar aggregates. From the value of the diffusion constant extrapolated at $c = 0$, the hydrodynamic radius R_H was also calculated according to the Stokes−Einstein relationship. We recall that for monodisperse and homogeneous spheres of radius R, one has $R = R_H = 1.29R_G$. For core−shell microstructures, e.g., obtained from amphiphilic block copolymers,[30,37,38] the ratio R_H/R_G has been found experimentally in the range 1−2. There, the hydrodynamic radius R_H is assumed to be the overall radius of the block copolymer micelle[39] and the shell thickness becomes $h = R_H - R_C$, where R_C is the radius of the core. Note that in general the determination of the core radius cannot be achieved by light scattering but requires additional techniques, such as cryogenic electron microscopy.

Small-angle X-ray scattering (SAXS) runs were performed at the Brookhaven National Laboratory (Brookhaven, USA) on the X21 and X3A2 beam lines. For the runs on X21, we used a wavelength $\lambda = 1.76$ Å for the incoming beam and the sample−detector distance of 1 m. With the detector in the off-center position, the accessible q-range was 0.01−0.4 Å^{-1}, with a resolution $\Delta q_{fwhm}/q$ of 1.25%. Δq_{fwhm} denotes here the full width at half-maximum of diffraction peaks characterizing

TABLE 1: Chemical Formula, Molecular Weight (M_w), Molar Volume (V_{mol}), and Coherent Neutron and X-ray Scattering Length Densities ($\rho_{N,X}$) for the Species Studied in This Work

species	chemical formula	M_w, g·mol^{-1}	V_{mol}, cm^3·mol^{-1}	ρ_N, 10^{10} cm^{-2}	ρ_X, 10^{10} cm^{-2}
acrylic acid	$CH_2CH-COOH$	72.06	47.8	+2.09	13.4
sodium acrylate	$CH_2CH-COO^-,Na^+$	94.04	33	+4.37	24.5
acrylamide in H_2O	$CH_2CH-CONH_2$	71.08	53.3	+1.86	12.0
acrylamide in D_2O	$CH_2CH-COND_2$	73.08	53.3	+4.19	12.0
yttrium hydroxyacetate	$Y(OH)_{1.7}(CH_3COO)_{1.3}$	194.58	50.0	+3.50	31.9
hydrogenated water	H_2O	18.02	18.02	−0.56	9.4
deuterated water	D_2O	20.02	18.02	+6.40	9.4

ordered structures. For the run on X3A2, the detector was located at 1.5 m, with $\lambda = 1.55$ Å and a q-range of interest of 0.008−0.27 Å^{-1}. The data were treated so as to remove the contribution of the glass capillary (diameter 1.5 mm) and that of the solvent. On the two beam lines, the wave-vector scale was calibrated against silver behenate powder. Thick films cast from the mixed polymer−nanoparticle solutions (thickness 0.1−1 mm) were directly taped on the sample holder.

Small-angle neutron scattering was performed at the Institute Laue-Langevin (Grenoble, France) on the D11 beam line. For SANS, polymer−nanoparticle hybrids were prepared with D_2O as a solvent for contrast reasons. On D11, the data collected at 1.1, 5, and 20 m cover a range in wave-vector of 2×10^{-3} to 0.35 Å^{-1}, with an incident wavelength of 8 Å and a wave-vector resolution $\Delta q/q$ of 10%. The spectra are treated according to the standard Institute Laue-Langevin procedures, and the scattering cross sections are expressed in cm^{-1}.

The molecular weight, volumes, and scattering length densities of the chemical species studied in this work are listed in Table 1. The data for the YHA nanoparticles were determined by contrast variation with the neutron technique. The stock solution prepared in H_2O at $c = 25.5$ wt % was diluted with D_2O down to a concentration of 1 wt %. Doing so, the scattering length density of the solvent ρ_S was allowed to change from $\rho_S = -0.56 \times 10^{10}$ to 6.2×10^{10} cm^{-2}. For $\rho_S = \rho_{YHA}$, it is predicted that the scattering intensity extrapolated to zero wave-vector should be zero.[40] Figure 2 displays the square root of the scattering intensity extrapolated at zero wave-vector and divided by the concentration for the series described previously, $[(1/c)\ d\sigma(q\rightarrow 0)/d\Omega]^{1/2}$. For the H_2O-rich mixtures, we also reversed the sign of the square root to emphasize the linear dependence as a function of ρ_S. $[(1/c)\ d\sigma(q\rightarrow 0)/d\Omega]^{1/2}$ vanishes at $\rho_N^{nano} = 3.50 \times 10^{10}$ cm^{-2}, which corresponds to the value of the average scattering length density for the nanoparticles. From ρ_N^{nano}, we also estimate the molar volume ($V_{mol} = 50.0$ cm^3·mol^{-1}) and X-ray scattering length density ($\rho_X^{nano} = 31.9 \times 10^{10}$ cm^{-2}) for the nanocolloids, using the expressions $\rho_{N,X} = b_{N,X}N_A/V_{mol}$. Here, b_N and $b_X = Zr_{el}$ are the neutron and X-ray scattering lengths of the elementary scatterer (Z denotes the number of electrons of this scatterer, N_A the Avogadro number, and r_{el} the electron radius).[40] As evidenced in Table 1, the YHA nanoparticles and the polymers have comparable neutron scattering densities with respect to D_2O, and thus both will contribute to the SANS cross-sections. By SAXS, the contrast of the inorganic part is much larger than that of the polymers, and as a result the nanoparticles will mainly dominate in X-ray.

II.3. Cryo-Transmission Electron Microscopy. Cryo-transmission electron microscopy (cryo-TEM) experiments were performed on polymer−nanoparticle solutions made at the preferred ratio and concentration $c = 0.2$ wt %. For cryo-TEM experiments, a drop of the solution was put on a TEM-grid covered by a 100 nm thick polymer perforated membrane. The drop was blotted with filter paper and the grid was quenched rapidly in liquid ethane to avoid the crystallization of the aqueous phase. The membrane was finally transferred into the vacuum column of a TEM-microscope (JEOL 1200 EX operating at 120 kV) where it was maintained at liquid nitrogen temperature. The magnification for the cryo-TEM experiments was selected at 20 000×.

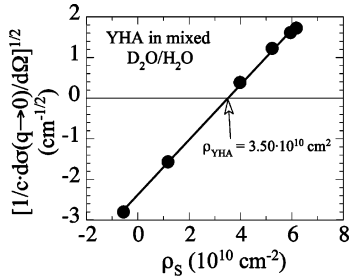

Figure 2. Square root of the SANS scattering intensity extrapolated at zero wave vector, $[(1/c)\ d\sigma(q\rightarrow 0)/d\Omega]^{1/2}$, for a series of dilute solutions made with mixed H_2O/D_2O solvent. The scattering length density of the solvent is allowed to change from $\rho_S = -0.56 \times 10^{10}$ cm^{-2} to 6.2×10^{10} cm^{-2}. $[(1/c)\ d\sigma(q\rightarrow 0)/d\Omega]^{1/2}$ cancels at $\rho_N^{nano} = 3.50 \times 10^{10}$ cm^{-2}, which is the value of the average scattering length density of the bare nanoparticles. Note that for the H_2O-rich mixtures we have reversed the sign of the square root to emphasize the linear dependence as a function of ρ_S.

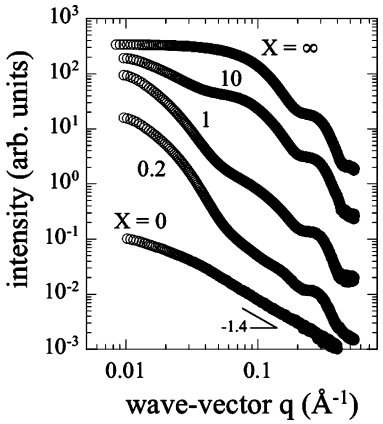

Figure 3. Small-angle X-ray scattering intensities obtained for mixed nanoparticle−polymer solutions at $c = 1$ wt % and X between 0 and 10. Each curve has been shifted for clarity. The upper curve for $X = \infty$ is the form factor of the YHA nanoparticles.[18]

III. Results and Discussion

III.1. Small-Angle X-ray Scattering. Figure 3 illustrates the SAXS intensities obtained at $c = 1$ wt % and X varying between 0 and ∞ (Figure 1). For the pure polymer solution ($X = 0$), the overall intensity is weak and it follows at high q a scaling law with an exponent of −1.4.[40,41] The data for $X = \infty$ represent the form factor of the YHA nanoparticles, obtained at slightly lower concentration ($c = 0.4$ wt %). The YHA form factor in Figure 3 exhibits a two-step decrease. The first decrease occurring at low q is associated with the overall size of the particle and provides a radius of gyration of $R_G^{nano} = 1.65$ nm.

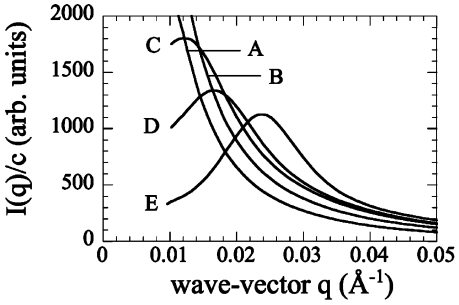

Figure 4. Normalized SAXS intensities for nanoparticle−polymer solutions at the concentrations $c = 2$ (A), 3.7 (B), 10.8 (C), 22 (D), and 40 wt % (E). The samples were obtained by slow evaporation of the solvent, starting with a solution prepared at $c = 2$ wt % and with PANa(5K)-*b*-PAM(30K) as complexing polymer. The samples at $c =$ 10.8 and 22 wt % are viscous liquids and that at 40 wt % is a gel.

At higher q, a shoulder shows up around 0.3 Å^{-1} that is the signature of a complex internal structure and that involves most likely two layers with different scattering length densities. For the intermediate X-values, $X = 0.2$, 1, and 10, the scattering cross-section is dominated by a strong forward scattering (i.e., as $q \rightarrow 0$). The forward scattering is indicative of the formation of large-scale aggregates. The radius of gyration associated with the intensity decrease at low q results in $R_G = 11$ nm, i.e., a value larger than that of the single nanoparticles by a factor of ∼5 (Table 1). From the X-dependence of the intensity, we confirm that the preferred mixing ratio for the YHA−diblock system is $X_P \sim 0.2$. We recall here that X_P is the ratio for which all the species present associate, yielding a maximum of the ($q \rightarrow 0$)-cross-section. Taking into account the molecular weight of the two components, $X_P = 0.2$ corresponds to ∼4 polymers per particle for PANa(5K)-*b*-PAM(30K) and to ∼2 polymers per particle for PANa(5K)-*b*-PAM(60K). In the sequel of this paper, we focus on this unique composition. Note finally the similarities in the q-dependencies between the data at $X = 10$ and ∞, especially at large wave-vectors. This shows that at high X there is a coexistence between unassociated nanoparticles and mixed aggregates.

Figure 4 shows the normalized intensities for mixed solutions at $c = 2$, 3.7, 10.8, 22, and 40 wt %. For these concentrations, the curves are labeled A, B, C, D, and E, respectively. The samples were obtained by slow evaporation of the solvent, starting from a solution prepared at $c = 2$ wt % and with PANa-(5K)-*b*-PAM(30K) as complexing agent. It is important to note here that the solutions at $c = 10.8$ and 22 wt % exhibit an increased viscosity as compared to that of the solvent. These two fluids remain, however, Newtonian. The system at $c = 40$ wt % on the contrary has the rheological properties of a strong gel.[42] The origin of the gel-like properties at high concentrations is discussed in the conclusion section. With increasing concentration in Figure 4, there is the development and growth of a structure peak that is the signature of the strong repulsive interactions between the hybrid aggregates. Located at a wave-vector $q_{Max}(c)$, the structure peak increases with increasing concentration. The quantity $2\pi/q_{Max}(c)$ is an estimate of the d spacing between aggregates. Figure 5 displays the evolution of the position of the structure peak in a double logarithmic representation as a function of the mass fraction. For the two systems PANa(5K)-*b*-PAM(30K)/YHA and PANa(5K)-*b*-PAM-(60K)/YHA studied, $q_{Max}(c)$ exhibits a power law with an exponent close to $^1/_3$. This power law is characteristic for strongly interacting spherical colloids. It is an indication too that the mixed aggregates preserved their structures as c is increased.

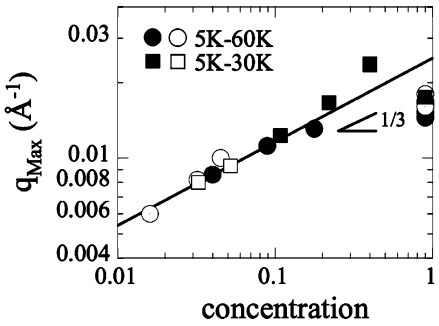

Figure 5. Evolution of the position of the structure peak $q_{Max}(c)$ in a double logarithmic representation for the PANa(5K)-*b*-PAM(30K)/YHA (squares) and PANa(5K)-*b*-PAM(60K)/YHA (circles) mixed systems as a function of the concentration. The solid (open) symbols refer to SAXS (SANS) experiments. $q_{Max}(c)$ exhibits a power law with an exponent close to $^1/_3$ in both cases.

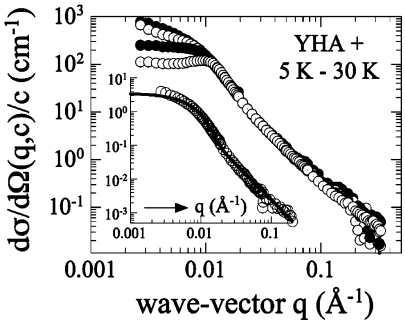

Figure 6. SANS scattering cross-sections obtained on PANa(5K)-*b*-PAM(30K)/YHA solutions at concentrations comprised between 0.5 and 5 wt %. The intensities have been divided by the concentration to emphasize the superposition of the data in the high q-range. Inset: Neutron scattering absolute intensity (cm^{-1}) of the mixed aggregates obtained at $c = 0.5$ wt %. As explained in the text, this intensity is proportional to the form factor of the hybrid aggregates. It is fitted by using an analytical expression developed for starlike objects, provided by eq 1 and shown as a continuous line.[44]

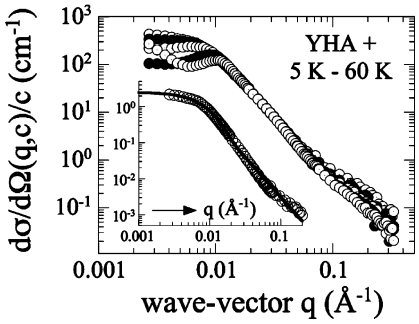

Figure 7. Same as Figure 6, but for PANa(5K)-*b*-PAM(60K)/YHA mixed systems.

III.2. Small-Angle Neutron Scattering. Figures 6 and 7 show the scattering cross-sections obtained by SANS on PANa-(5K)-*b*-PAM(30K)/YHA and PANa(5K)-*b*-PAM(60K)/YHA solutions at concentrations comprised between 0.5 and 5 wt %. The intensities have been divided by the concentration to emphasize the superposition of the data in the high q-range. This approach is required to separate the contributions between the form and the structure factors of the hybrid aggregates. The intensities at low concentration, here $c = 0.5$ wt %, are proportional to the form factor (see insets in Figures 6 and 7). As for the SAXS data, this form factor shows a significant forward scattering. However, at high wave-vectors, it is followed by a decrease in the form of power law. This latter regime is different from that observed in SAXS (Figure 3) and it is due

TABLE 2: Characteristic Sizes for Poly(acrylic acid)-*b*-poly(acrylamide) Block Copolymers, Yttrium Hydroxyacetate Nanoparticles, and Mixed Polymer−Nanoparticle Aggregates

colloidal species	R_H (nm)	R_G (nm)
PANa(5K)-*b*-PAM(30K)	5.5 (*l*)	n.d.
PANa(5K)-*b*-PAM(60K)	7.9 (*l*)	
YHA−nanoparticle	∼2 (*l*)	1.82 (*n*) 1.65 (*x*)
mixed aggregate in:		
Figure 4	34 (*l*)	17.2 (*l*); 11.0 (*x*)
Figure 8	40 (*l*)	22.7 (*n*)
Figure 9	36 (*l*)	18.2 (*n*)

to the different scattering contrasts for the core and for the shell with respect to the two techniques. The asymptotic behaviors for the form factors are similar to those found in polymer stars, especially with polymer stars with a large number of arms.[43,44] Following Grest et al.,[44,45] the scattering intensity for starlike objects can be approximated by

$$\frac{d\sigma}{d\Omega}(q,c\ll 1) = \alpha \exp\left(-\frac{q^2 {R_G}^2}{3} + \beta \frac{\sin(\mu \tan^{-1}(q\xi))}{q\xi(1+q^2\xi^2)^{\mu/2}}\right) \quad (1)$$

The first term in the right-hand side of eq 1 accounts for the overall size of the colloidal particle and determines its gyration radius R_G. The second term is the Fourier transform of the monomer−monomer correlation function within the corona in agreement with the Daoud and Cotton Model.[46] In eq 1, α and β are prefactors, and ξ is the average blob size in the corona. Effective at large q, the second contribution decreases as $q^{-\mu-1}$. For Gaussian chains, $\mu = 1$, and for chains in good solvent conditions, $\mu = {}^2/_3$. As shown in the insets, the overall q-dependence of the intensity is well accounted for by eq 1. Adjustable parameters are α, R_G, β, ξ, and μ. We obtained radii of gyration $R_G = 22.7$ and 18.2 nm, a power law exponent of -2 in the high q-region (i.e., $\mu = 1$ in eq 1) and $\xi = 15-20$ nm. In Figures 6 and 7, the superimposition of the intensities in the range $0.01-0.4$ Å^{-1} suggests that the internal structure of the aggregates is not altered by the removal of the solvent, and the subsequent increase of the weight and volume concentration. The shift of the structure factor to higher wave-vectors is observed for the two systems with increasing concentration. The $q_{Max}(c)$-values obtained by SANS have been included in Figure 5, and they are found to align with the SAXS data. The straight line in Figure 5 is obtained by using the expression $q_{Max}(c) = q_0 c^{1/3}$, with $q_0 = 0.025$ Å^{-1}. The two systems, PANa(5K)-*b*-PAM(30K)/YHA and PANa(5K)-*b*-PAM(60K)/YHA, follow nearly the same behavior, a finding that is in agreement with the fact that both types of aggregates have similar hydrodynamic and gyration radii (Table 2).

III.3. Association Morphology between Polymers and Nanoparticles. Figure 8a displays a picture obtained by cryo-TEM of the PANa(5K)-*b*-PAM(60K)/YHA solution at $c = 1$ wt % and $X = 0.2$. Prior to the cryo-TEM experiments, the solution was characterized by static and dynamic light scattering, yielding for the gyration and hydrodynamic radii $R_G = 17.2$ nm and $R_H = 33.5$ nm (see Table 2). The field covered on the graph is $\sim 600 \times 600$ nm^2 and was obtained with a 20 000× magnification. This magnification allows us to clearly distinguish dark patches on a gray background, with radii comprised between 5 and 15 nm. An image analysis on 74 patches provides the size distribution of these patches (Figure 8b). The distribution is found to be described by a log-normal function with an average radius $R_C = 8.3 \pm 0.2$ nm and a polydispersity $s = 0.16 \pm 0.02$. Since the YHA nanoparticles have the largest

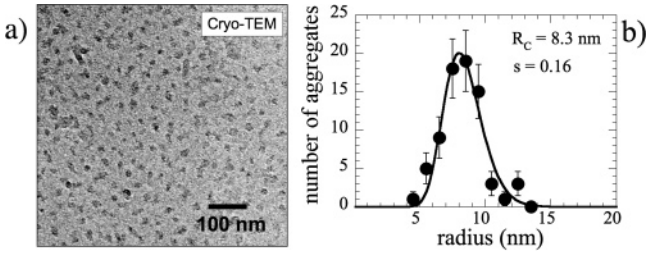

Figure 8. (a) Cryo-TEM image of mixed aggregates obtained by complexation between PANa(5K)-*b*-PAM(60K) and YHA. The total concentration is $c = 1$ wt % and $X = X_P$ ($=0.2$). The field covered on the graph is $\sim 600 \times 600$ nm^2. The patches delimitate the contours of the cores, as discussed in the text. (b) Size distribution of the dark patches identified in panel a. The continuous line results from a fitting procedure, using a log-normal function with average radius $R_C = 8.3 \pm 0.2$ nm and polydispersity $s = 0.16 \pm 0.02$.

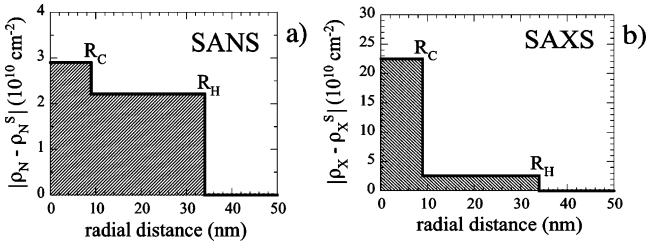

Figure 9. SANS (a) and SAXS (b) contrasts of the YHA−copolymer supermicellar aggregates as determined from the comparison between scattering techniques and cryo-TEM.

electronic density from all the species present, we can assume that the patches in Figure 8a delimitate the cores of the hybrid aggregates (polymers are not visible with this technique). That the cores are close to each other comes from the fact that the colloids are located at different heights within the ∼200 nm thick film studied by cryo-TEM. From the value of $R_C = 8.3$ nm, we can derive two quantities which are relevant for the complexes: the thickness of the neutral polymer brush surrounding the cores, $h = R_H - R_C = 25$ nm, and the aggregation numbers, expressed here in terms of the number of nanoparticles per aggregate. For this latter determination, the expression $N_{Agg} = \phi_C (R_C/R)^3$ is used[26,28] where ϕ_C ($=0.4$) is the volume fraction of particles in the core and R the radius of a single particle. We obtain $N_{Agg} = 92$, in good agreement with former determinations.[18,19] Panels a and b in Figure 9 illustrate respectively the SANS and SAXS contrasts for core−shell aggregates with core radius and shell thickness as determined from the previous analysis.

III.4. Thick Films Cast from Solutions. Solid thick films made from PANa-*b*-PAM/YHA were cast from dilute solutions in a two-step process. In the first step, an ultrafiltration cell allows us to reach a range around 10 wt %, where the liquid becomes noticeably viscous. Then, the films are cast following the solvent evaporation protocols developed for amphiphilic copolymers.[33,34] Figure 10a displays a picture of a macroscopic film obtained from PANa(5K)-*b*-PAM(60K)/YHA. With a thickness evaluated around 100 μm, the film is transparent and brittle. It shows the same mechanical properties as a poly(acrylamide) film made in the same conditions. We have checked that without addition of polymers, the YHA nanoparticles alone do not form a film, but instead a white powder (Figure 10b). To check the structure of the composite films, the PANa-*b*-PAM/YHA thick films were investigated by SAXS. As illustrated in Figure 11, the data of a solid-state sample exhibit a correlation peak around 0.02 Å^{-1} associated with a *d*-spacing of ∼320 Å. This peak results from the correlation

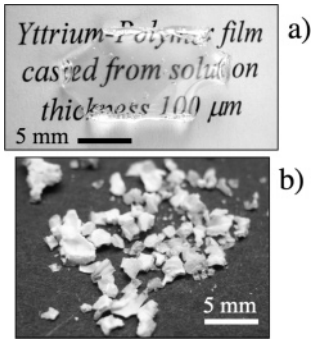

Figure 10. (a) Image of a PANa(5K)-*b*-PAM(60K)/YHA thick film obtained by casting. The film is 100 μm thick, transparent, and brittle. (b) Powder obtained in the same casting conditions as in panel a, and starting from a YHA solution with no polymer added.

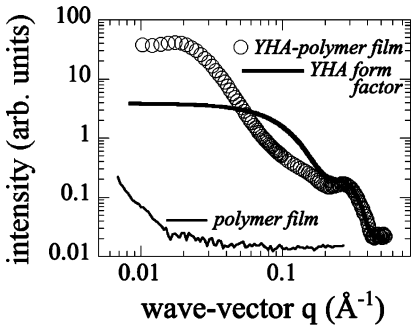

Figure 11. Comparison between SAXS intensities obtained from a composite film (open symbols), from a YHA−nanoparticle solution (form factor, thick line), and from a poly(acrylamide) film (thin line). The structure peak observed for the composite film at $q \sim 0.02$ Å^{-1} results from the correlation between the YHA clusters. Note the superimposition observed above 0.2 Å^{-1} between the film intensity and the particle form factor.

between the YHA clusters which have sustained the solvent evaporation process. The YHA cores can now be considered as dispersed inclusions in a solid PAM matrix. Also displayed in the figure is the result of an experiment with a PAM film without added particle. In this case, the scattering is flat and no structure peak is visible. In Figure 11, the scattering cross-section obtained for the thick film compares very well with the form factor of the nanoparticles, especially at large wave-vector. The superimposition observed above 0.2 Å^{-1}, i.e., on a local scale, confirms the presence of the nanoparticles in the film. Finally, we have included in Figure 6 the q_{Max}-values observed on several films, that is for $c \rightarrow 1$. We have found systematically $q_{Max}(c \rightarrow 1)$ between 0.015 and 0.02 Å^{-1}, instead of the 0.025 Å^{-1} extrapolated from the dilute solution scaling. This deviation could be explained by a partial reorganization of the cores during the late stages of the solvent evaporation. In conclusion, we confirm that the nanocomposite thick films achieved by this technique contain 20% by weight of nanoparticles and ∼70−80% of polymers. These latter percentages depend on the number of unbound water molecules remaining in the films.

IV. Conclusion

In the present paper, we have shown that the inherent instability of inorganic nanoparticle sols in general may be resolved by complexation with oppositely charged ion-containing polymers. In addition to our previous contributions on nanoparticle−polymer self-assemblies,[18,21] here we investigate a new property for these aggregates, namely their stability as a function of the concentration and their propensity to build nanocomposite films. We have found that the mixed aggregates can sustain the solvent removal up to the solid state. Solid films with thicknesses up to several hundreds of microns were cast from solutions and the structure of the complexes remains unchanged during film casting.

In the dilute regime, X-ray and neutron scattering have revealed the form factor of the supermicellar aggregates. The core−shell microstructure of the supermicellar aggregates was derived from a combination of the scattering (light, X-ray, neutron) and electron microscopy experiments, as well as from a quantitative determination of the different scattering length densities. To fit the SANS data in the dilute regime, we used well-established phenomenological equations derived for polymer stars.[40,44,45] In the intermediate regime of concentration, we have observed around $c = 10$ wt % viscous liquids, and at $c = 40$ wt % viscoelastic gels. The gel-like properties of the latter solutions result from the high packing fraction of the supermicellar aggregates and from the deformation of the neutral brush (increasing then the contribution to the elastic modulus). On the whole concentration range, which is between 1 and ∼90 wt %, the position of the primary structure peak revealed in the scattering intensities scales with the total concentration according to $c^{1/3}$, which is characteristic for aggregates with fixed aggregation number and local spherical symmetry. From their core−shell microstructure as well as from their concentration behaviors, the YHA−copolymer mixed micelles bear strong similarities with the amphiphilic block copolymers in aqueous solutions.[30]

Acknowledgment. We thank Yoann Lalatonne, Julian Oberdisse, and Amit Sehgal for many useful discussions. Mathias Destarac, Annie Vacher, and Marc Airiau from the Centre de Recherches d'Aubervilliers (Rhodia, France) are acknowledged for providing us with polymers and for the Cryo-TEM images of the mixed aggregates. This research is supported by Rhodia and by the Centre de la Recherche Scientifique in France.

References and Notes

(1) Lewis, J. A. *J. Am. Ceram. Soc.* **2000**, *83*, 2341−2359.
(2) Sanchez, C.; Soler-Illia, G. J. A. A.; Ribot, F.; Grosso, D. *C. R. Chim.* **2003**, *6*, 1131
(3) Pankhurst, Q. A.; Connolly, J.; Jones, S. K.; Dobson, J. *J. Phys. D*: *Appl. Phys.* **2003**, *36*, R167 − R181.
(4) Michalet, X.; Pinaud, F. F.; Bentolila, L. A.; Tsay, J. M.; Doose, S.; Li, J. J.; Sundaresan, G.; Gambhir, S. S.; Weiss, S. *Science* **2005**, *307*, 538.
(5) Torchilin, V. T. *Adv. Drug Delivery Rev.* **2002**, *54*, 235.
(6) Gould, P. *Mater. Today* **2004**, *7*, 36.
(7) Sonvico, F.; Mornet, S.; Vasseur, S.; Dubernet, C.; Jaillard, D.; Degrouard, J.; Hoebeke, J.; Duguet, E.; Colombo, P.; Couvreur, P. *Bioconj. Chem.* **2005**, *16*, 1181.
(8) Wang, Y.; Teng, X.; Wang, J. S.; Yang, H. *Nano Lett.* **2003**, *3*, 789.
(9) Chen, X. Y.; Armes, S. P.; Greaves, S. J.; Watts, J. F. *Langmuir* **2004**, *20*, 587.
(10) Ai, H.; Flask, C.; Weinberg, B.; Shuai, X.; Pagel, M.; Farrell, D.; Duerk, J.; Gao, J. *Adv. Mater.* **2005**, *17*, 1949.
(11) Ohno, H.; Koh, K.-M.; Tsuji, Y.; Fukuda, T. *Macromolecules* **2002**, *35*, 8989.
(12) Selvan, S. T.; Spatz, J.; Klok, H.-A.; Möller, M. *Adv. Mater.* **1998**, *10*, 132.
(13) Sohn, B.-H.; Choi, J.-M.; Yoo, S. I.; Yun, S.-H.; Zin, W.-C.; Jung, J. C.; Kanehara, M.; Hirata, T.; Teranishi, T. *J. Am. Chem. Soc.* **2003**, *125*, 6368.
(14) Chiu, J. J.; Kim, B. J.; Kramer, E. J.; Pine, D. J. *J. Am. Chem. Soc.* **2005**, *127*, 5036.
(15) Zhang, Q.; Xu, T.; Butterfield, D.; Missner, M. J.; Ryu, D. Y.; Emrick, T.; Russell, T. P. *Nano Lett.* **2005**, *5*, 357.
(16) Lecommandoux, S.; Sandre, O.; Chécot, F.; Rodriguez-Hernandez, J.; Perzynski, R. *Adv. Mater.* **2005**, *17*, 712.

(17) Lin, Y.; Böker, A.; He, J.; Still, K.; Xiang, H.; Abetz, C.; Li, X.; Wang, J.; Emrick, T.; L.ong, S.; Wang, Q.; Balazs, A.; Russell, T. P. *Nature* **2005**, *343*, 55.

(18) Yokota, K.; Morvan, M.; Berret, J.-F.; Oberdisse, J. *Europhys. Lett.* **2004**, *69*, 284−290.

(19) Berret, J.-F.; Yokota, K.; Morvan, M. *Soft Mater*. **2004**, *2*, 71−84.

(20) Berret, J.-F.; Gazeau, F.; Kharrat, D. E.; Sandre, O. *Superparamagnetic Nanoparticles and Oppositely Charged Polymers: Design of New Contrast Agents for Magnetic Resonance Imaging*; MHD Pamir Conference, 2005, Riga, Litvia.

(21) Berret, J.-F.; Schonbeck, N.; Gazeau, F.; Kharrat, D. E.; Sandre, O.; Vacher, A.; Airiau, M. *J. Am. Chem. Soc.* **2006**, *128*, 1555.

(22) Sehgal, A.; Lalatonne, Y.; Berret, J.-F.; Morvan, M. *Langmuir* **2005**, *21*, 9359.

(23) Bronich, T. K.; Cherry, T.; Vinogradov, S.; Eisenberg, A.; Kabanov, V. A.; Kabanov, A. V. *Langmuir* **1998**, *14*, 6101.

(24) Hervé, P.; Destarac, M.; Berret, J.-F.; Lal, J.; Oberdisse, J.; Grillo, I. *Europhys. Lett.* **2002**, *58*, 912.

(25) Berret, J.-F.; Cristobal, G.; Hervé, P.; Oberdisse, J.; Grillo, I. *Eur. J. Phys. E* **2002**, *9*, 301.

(26) Berret, J.-F.; Hervé, P.; Aguerre-Chariol, O.; Oberdisse, J. *J. Phys. Chem. B* **2003**, *107*, 8111.

(27) Berret, J.-F.; Vigolo, B.; Eng, R.; Hervé, P.; Grillo, I.; Yang, L. *Macromolecules* **2004**, *37*, 4922.

(28) Berret, J.-F. *J. Chem. Phys.* **2005**, *123*, 164703.

(29) Yokota, K.; Berret, J.-F.; Tolla, B.; Morvan, M. U.S. provisional patent application 2004, RD 04004 (serial number 60/540 430).

(30) Riess, G. *Prog. Polym. Sci.* **2003**, *28*, 1107.

(31) Discher, B. M.; Won, Y. Y.; Ege, D. S.; Lee, J. C.-M.; Bates, F. S.; Discher, D.; Hammer, D. A. *Science* **1999**, *284*, 1143.

(32) Hantley, K. J.; Lodge, T. P.; Huang, G.-I. *Macromolecules* **2000**, *33*, 5918.

(33) Bendejacq, D.; Ponsinet, V.; Joanicot, M.; Loo, Y.-L.; Register, R. A. *Macromolecules* **2002**, *35*, 6645.

(34) Bendejacq, D.; Ponsinet, V.; Joanicot, M.; Vacher, A.; Airiau, M. *Macromolecules* **2003**, *36*, 7289.

(35) Taton, D.; Wilczewska, A.-Z.; Destarac, M. *Macromol. Rapid Commun.* **2001**, *22*, 1497.

(36) Destarac, M.; Bzducha, W.; Taton, D.; Gauthier-Gillaizeau, I.; Zard, S. Z. *Macromol. Rapid Commun.* **2002**, *23*, 1049.

(37) Förster, S.; Zisenis, M.; Wenz, E.; Antonietti, M. *J. Chem. Phys* **1996**, *104*, 9956.

(38) Willner, L.; Pope, A.; Allgaier, J.; Monkenbusch, M.; Lindner, P.; Richter, D. *Europhys. Lett.* **2000**, *51*, 628.

(39) Pham, Q. T.; Russel, W. B.; Thibeault, J. C.; Lau, W. *Macromolecules* **1999**, *32*, 2996.

(40) Lindner, P.; Zemb, T. *Neutrons, X-rays and Light*: *Scattering Methods Applied to Soft Condensed Matter*; Elsevier: Amsterdam, The Netherlands, 2002.

(41) Pedersen, J. S.; Svaneborg, C. *Curr. Opin. Colloid Interface Sci.* **2002**, *7*, 158.

(42) Larson, R. G. *The Structure and Rheology of Complex fluids*; Oxford University Press: New York, 1999.

(43) Dozier, W. D.; Huang, J. S.; Fetters, L. J. *Macromolecules* **1991**, *24*, 2810.

(44) Grest, G. S.; Fetters, L. J.; Huang, J. S. *Adv. Chem. Phys.* **1996**, *19*, 67.

(45) Séréro, Y.; Aznar, R.; Porte, G.; Berret, J.-F.; Calvet, D.; Collet, A.; Viguier, M. *Phys. Rev. Lett.* **1998**, *81*, 5584.

(46) Daoud, M.; Cotton, J.-P. *J. Phys. France* **1982**, *43*, 531.